

A novel approach for fusion of heterogeneous sources of data

Mostafa Reisi Gahrooei¹, Hao Yan², Kamran Paynabar¹, Jianjun Shi¹

¹Georgia Institute of Technology, Atlanta, GA 30332, USA

²Arizona State University, Tempe, AZ 85281, USA

Abstract

With advancements in sensor technology, heterogeneous sets of data such as those containing scalars, waveform signals, images, and even structured point clouds, are becoming increasingly popular. Developing statistical models based on such heterogeneous sets of data to represent the behavior of an underlying system can be used in the monitoring, control, and optimization of the system. Unfortunately, available methods only focus on the scalar and curve data and do not provide a general framework for integrating different sources of data to construct a model. This paper addresses the problem of estimating a process output, measured by a scalar, curve, image, or structured point cloud by a set of heterogeneous process variables such as scalar process setting, sensor readings, and images. We introduce a general multiple tensor-on-tensor regression (MTOT) approach in which each set of input data (predictor) and output measurements are represented by tensors. We formulate a linear regression model between the input and output tensors and estimate the parameters by minimizing a least square loss function. In order to avoid overfitting and reduce the number of parameters to be estimated, we decompose the model parameters using several bases that span the input and output spaces. Next, we learn the bases and their spanning coefficients when minimizing the loss function using a block coordinate descent algorithm combined with an alternating least square (ALS) algorithm. We show that such a minimization has a closed-form solution in each iteration and can be computed very efficiently. Through several simulation and case studies, we evaluate the performance of the proposed method. The results reveal the advantage of the proposed method over some benchmarks in the literature in terms of the mean square prediction error.

1 Introduction

With advancements in sensor technology, heterogeneous sets of data containing scalars, waveform signals, images, etc. are more and more available. For example, in semiconductor manufacturing, machine/process settings (scalar variables), sensor readings in chambers (waveform signals), and wafer shape measurements (images) may be collected to model and monitor the process. In this article, we refer to non-scalar variables as high-dimensional (HD) variables. Analysis and evaluation of such heterogeneous data sets can benefit many applications, including manufacturing processes (Szatvanyi *et al.*, 2006; Wójcik & Kotyra, 2009), food industries (Yu & MacGregor, 2003), medical decision-making (Bellon *et al.*, 1995), and structural health monitoring (Balageas *et al.*, 2010). Specifically, analysis of such data may lead to the construction of a statistical model that estimates a variable (including HD) based on several other variables (regression model). Unfortunately, most works in regression modeling only consider scalars and waveform signals (Liang *et al.*, 2003; Ramsay & Silverman, 2005; Fan *et al.*, 2014; Luo & Qi, 2017), without including images or structured point clouds. However, in several applications, images or structured point clouds are available. For example, materials scientists are interested in constructing a link between process variables, e.g., the temperature and pressure under which a material is operating, and the microstructure of the material (Khosravani *et al.*, 2017), which is often represented by an image or a variation of the microstructure image obtained by two-point statistics. Generating such a linkage model requires regression analysis between scalar and waveform process variables as inputs and an image. For more detailed information and a case study, please refer to (Gorgannejad *et al.*, 2018).

As another example, in semiconductor manufacturing, overlay errors (defined as the difference between in-plane displacements of two layers of a wafer) are directly influenced by the shape of the wafer before the lithographic process. In this process, both the wafer shape and the overlay error (in the x and y directions) can be represented as images as shown in Figure 1. Prediction of the overlay error across a wafer based on the wafer shape can be fed forward to exposure tools for specific corrections (Turner *et al.*, 2013). In order to predict the overlay error based on the wafer shape deformation, an image-on-image statistical model is required to capture the correlation between the wafer overlay and shape.

In addition to the space and computational issues caused by the large size of the HD variables,

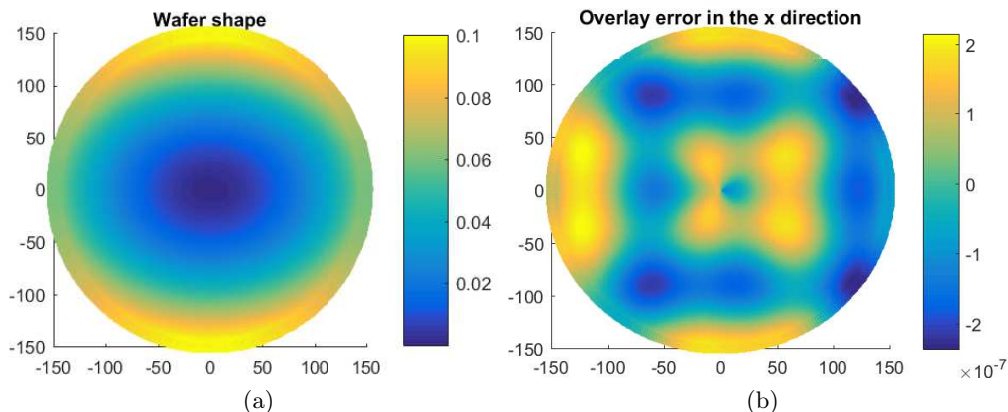


Figure 1: Examples of the (a) wafer shape and (b) x coordinate overlay error. All measurements are in millimeters (mm). The wafer in (a) has an overall bow shape, with several high-order waveform patterns that cannot be seen. Figure (b) represents the misalignment of two layers in the x coordinate. The dark blue represents a large error in the negative direction of the x coordinate, and light yellow represents a large error in the positive direction of the x coordinate.

the challenge of developing an accurate model for a process with a heterogeneous group of variables is twofold: Integrating variables of different forms (e.g., scalars, images, curves) while capturing their “within” correlation structure. Mishandling this challenge can lead to an overfitted, inaccurate model. The regular regression approach that considers each observation within an HD variable as an independent predictor excessively increases the number of covariates in comparison to the sample size ($p \gg n$) and ignores the correlation between the observations. Consequently, this method may cause severe overfitting and produce inaccurate predictions. Principle component regression (PCR) alleviates the problem by first reducing the dimension of both the input variables and the output. Nevertheless, PCR fails to exploit the structure of images or point clouds. Furthermore, PCR determines the principle components (PCs) of the inputs and the outputs separately from each other without considering the interrelationship between them. Functional data analysis, specifically the functional regression model (FRM), has become popular in recent years due to its built-in data reduction functionality and its ability to capture nonlinear correlation structures (Liang *et al.*, 2003; Ramsay & Silverman, 2005; Yao *et al.*, 2005; Fan *et al.*, 2014; Ivanescu *et al.*, 2015; Luo & Qi, 2017). However, FRM requires a set of basis functions that is usually specified based on domain knowledge rather than a data-driven approach. Recently, Luo & Qi (2017) proposed an approach that can combine several profiles and scalars to predict a curve, while learning the bases that span the input and output spaces. Nevertheless, it is not clear how to extend this approach to other

forms of data effectively.

In the past few years, multilinear algebra (and, in particular, tensor analysis) has shown promising results in many applications from network analysis to process monitoring (Sun *et al.*, 2006; Sapienza *et al.*, 2015; Yan *et al.*, 2015). Nevertheless, only a few works in the literature use tensor analysis for regression modeling. Zhou *et al.* (2013) has successfully employed tensor regression using PARAFAC/CANDECOMP (CP) decomposition to estimate a scalar variable based on an image input. The CP decomposition approximates a tensor as a sum of several rank-1 tensors (Kiers, 2000). Zhou *et al.* (2013) further extended their approach to a generalized linear model for tensor regression in which the scalar output follows any exponential family distribution. Li *et al.* (2013) performed tensor regression with scalar output using Tucker decomposition. Tucker decomposition is a form of higher order PCA that decomposes a tensor into a core tensor multiplied by a matrix along each mode (Tucker, 1963). CP decomposition is a special case of Tucker decomposition that assumes the same rank for all the basis matrices. Yan *et al.* (2017) performed the opposite regression and estimated point cloud data using a set of scalar process variables. Recently, Lock (2017) developed a tensor-on-tensor regression (TOT) approach that can estimate a tensor using a tensor input while learning the decomposition bases. However, several limitations in TOT should be addressed. First, TOT uses CP decomposition, which restricts both the input and output bases to have exactly the same rank (say, R). This restriction may cause over- or under-estimation when the input and the output have different ranks. For example, when estimating an image based on few scalar inputs, the rank of the output can be far larger than the input matrix. Second and more importantly, this approach can only take into account a single tensor input and cannot be used effectively when multiple sources of input data with different dimensions and forms (e.g., a combination of scalar, curve, and image data) are available. The extension of TOT to multiple tensor inputs generates a significant challenge due to the first limitation previously mentioned. Because the output and the inputs should have the same rank, extending the TOT approach to multiple tensor inputs as well requires all the inputs to have the same rank (which is equal to the rank of the output). However, this means that in certain situations, such as when scalar and image inputs exist, one of the inputs should take the rank of the other, causing a severe underfitting or overfitting problem. One approach to allow multiple forms of data in TOT is to combine all the data into one single input tensor, e.g., an image and scalar input being merged by transforming each scalar

value into a constant image. However, this approach generates a few issues: First, it significantly increases the size of the data, and second, it masks the separate effect of each input on the output due to the fusion of inputs. Furthermore, in situations in which the dimension of modes does not match (for example, a curve input with 60 observed points and an image of size 50x50), merging data into one tensor requires a method for dimension matching. Finally, the TOT approach fails to work on tensors of moderate size (e.g., on the image data of size 20000 pixels used in our case study) due to its high space complexity.

The overarching goal of this paper is to overcome the limitations of the previous methods, such as PCR, FRMs, and TOT, by constructing a unified regression framework that estimates a scalar, curve, image, or structured point cloud based on a heterogeneous set of (HD) input variables. This will be achieved by representing the output and each group of input variables as separate tensors and by developing a multiple tensor-on-tensor regression (MTOT). To avoid overfitting and estimating a large number of parameters, we perform Tucker decomposition on each group of inputs' parameters using one set of bases to expand each of the input spaces and another set of bases to span the output space. We obtain the input bases by performing Tucker decomposition on the input tensors, then define a least square loss function to estimate the decomposition coefficients and output bases. To ensure uniqueness, we impose an orthonormality constraint over the output bases when minimizing the loss function and show a closed-form solution for both the bases and the decomposition coefficient in each iteration of our algorithm. This approach not only performs dimension reduction similar to PCR, but it also learns the output bases in accordance with the input space. Furthermore, the use of tensors to represent the data preserves the structure of an image or structured point cloud.

The rest of the article is organized as follows: In Section 2, we introduce notations and the multilinear algebra concepts used in the paper. In Section 3, we formulate the multiple tensor-on-tensor regression model and illustrate the closed-form solution for estimating the parameters. In Section 4, we describe four simulation studies. The first simulation study combines a profile and scalar data to estimate a profile output. This simulation study is particularly considered to compare MTOT to the available methods in functional regression. The second and third simulation studies contain images or point clouds either as the input or output. The fourth simulation considers estimating a nonsmooth profile using a set of scalar inputs. In each simulation study, we compare

the performance of the proposed method with benchmarks in terms of (standardized) mean square prediction errors (MSPE). A case study on predicting the overlay errors based on the wafer shape is conducted in Section 5. Finally, we summarize the paper in Section 6.

2 Tensor Notation and Multilinear Algebra

In this section, we introduce the notations and basic tensor algebra used in this paper. Throughout the paper, we denote a scalar by a lower or upper case letter, e.g., a or A ; a vector by a boldface lowercase letter and a matrix by a boldface uppercase letter, e.g., \mathbf{a} and \mathbf{A} ; and a tensor by a calligraphic letter, e.g., \mathcal{A} . For example, we denote an order- n tensor by $\mathcal{R} \in \mathbb{R}^{I_1 \times I_2 \times \cdots \times I_n}$, where I_i is the dimension of the i^{th} mode of tensor \mathcal{R} . We also denote a mode- j matricization of tensor \mathcal{R} as $\mathbf{R}_{(j)} \in \mathbb{R}^{I_j \times I_{-j}}$, whose columns are the mode- j fibers of the corresponding tensor \mathcal{R} , and $I_{-j} = I_1 \times I_2 \times \cdots \times I_{j-1} \times I_{j+1} \times \cdots \times I_n$. We also define a more general matricization of a tensor $\mathcal{T} \in \mathbb{R}^{P_1 \times \cdots \times P_l \times Q_1 \times \cdots \times Q_d}$ as follows: Let $\mathbb{I} = \{I_1, I_2, \dots, I_l\}$ and $\mathbb{Q} = \{Q_1, Q_2, \dots, Q_d\}$ be two sets that partition the set $\{I_1, I_2, \dots, I_l, Q_1, Q_2, \dots, Q_d\}$, which contains the dimensions of the modes of the tensor \mathcal{T} . Then, the matricized tensor is specified by $\mathbf{T}_{(\mathbb{I} \times \mathbb{Q})} \in \mathbb{R}^{P \times Q}$, where $P = \prod_{i=1}^l P_i$ and $Q = \prod_{i=1}^d Q_i$, and

$$(\mathbf{T}_{(\mathbb{I} \times \mathbb{Q})})_{ij} = \mathcal{T}_{p_1 \cdots p_l q_1 \cdots q_d},$$

where $i = 1 + \sum_{r=1}^l \prod_{n=1}^r P_n (p_n - 1)$ and $j = 1 + \sum_{r=1}^d \prod_{n=1}^r Q_n (q_n - 1)$. For simplicity of notation, we will denote $\mathbf{T}_{(\mathbb{I} \times \mathbb{Q})}$ as \mathbf{T} .

The Frobenius norm of a tensor \mathcal{R} can be defined as the Frobenius norm of any matricized tensor, e.g., $\|\mathcal{R}\|_F^2 = \|\mathbf{R}_{(1)}\|_F^2$. The mode- j product of a tensor \mathcal{R} by a matrix $\mathbf{A} \in \mathbb{R}^{L \times I_j}$ is a tensor in $\mathbb{R}^{I_1 \times I_2 \times \cdots \times I_{j-1} \times L \times I_{j+1} \times \cdots \times I_n}$ and is defined as

$$(\mathcal{R} \times_j \mathbf{A})_{i_1, i_2, \dots, i_{j-1}, l, i_{j+1}, \dots, i_n} = \sum_{i_j=1}^{I_j} \mathcal{R}_{i_1, \dots, i_j, \dots, i_n} \mathbf{A}_{l, i_j}.$$

The Tucker decomposition of a tensor \mathcal{R} decomposes the tensor into a core tensor $\mathcal{C} \in \mathbb{R}^{P_1 \times P_2 \times \cdots \times P_n}$ and n orthogonal matrices $\mathbf{U}_i \in \mathbb{R}^{I_i \times P_i}$ ($i = 1, 2, \dots, n$) so that $\mathcal{R} = \mathcal{C} \times_1 \mathbf{U}_1 \times_2 \mathbf{U}_2 \times_3 \cdots \times_n \mathbf{U}_n$. The dimensions of the core tensor \mathcal{C} is smaller than \mathcal{A} , i.e., $P_j \leq I_j$ ($j = 1, 2, \dots, n$). Furthermore, the Kronecker product of two matrices $\mathbf{A} \in \mathbb{R}^{m \times n}$ and $\mathbf{B} \in \mathbb{R}^{r \times s}$ is denoted as $\mathbf{A} \otimes \mathbf{B} \in \mathbb{R}^{mr \times ns}$

and is obtained by multiplying each element of matrix \mathbf{A} to the entire matrix \mathbf{B} :

$$\mathbf{A} \otimes \mathbf{B} = \begin{bmatrix} a_{11}\mathbf{B} & \dots & a_{1n}\mathbf{B} \\ \vdots & \ddots & \vdots \\ a_{m1}\mathbf{B} & \dots & a_{mn}\mathbf{B} \end{bmatrix}.$$

We link the tensor multiplication with the Kronecker product using the Proposition 1.

Proposition 1. Let $\mathbf{U}_i \in \mathbb{R}^{P_i \times \tilde{P}_i}$ ($i = 1, \dots, l$) and $\mathbf{V}_i \in \mathbb{R}^{Q_i \times \tilde{Q}_i}$ ($i = 1, \dots, d$), and let $\mathcal{T} \in \mathbb{R}^{P_1 \times \dots \times P_l \times Q_1 \times \dots \times Q_d}$ and $\mathcal{C} \in \mathbb{R}^{\tilde{P}_1 \times \dots \times \tilde{P}_l \times \tilde{Q}_1 \times \dots \times \tilde{Q}_d}$, then

$$\begin{aligned} \mathcal{T} &= \mathcal{C} \times_1 \mathbf{U}_1 \times \mathbf{U}_2 \times_3 \dots \times_l \mathbf{U}_l \times_{l+1} \mathbf{V}_1 \times_{l+2} \dots \times_{l+d} \mathbf{V}_d \iff \\ \mathbf{T} &= (\mathbf{U}_l \otimes \mathbf{U}_{l-1} \otimes \dots \otimes \mathbf{U}_1) \mathbf{C} (\mathbf{V}_d \otimes \mathbf{V}_{d-1} \otimes \dots \otimes \mathbf{V}_1)^\top, \end{aligned}$$

where $\mathcal{C} \in \mathbb{R}^{\tilde{P} \times \tilde{Q}}$ is an unfold of the core tensor \mathcal{C} with $\tilde{P} = \prod_{j=1}^l \tilde{P}_j$ and $\tilde{Q} = \prod_{j=1}^d \tilde{Q}_j$.

The proof of this proposition can be found in (Kolda, 2006). Finally, the contraction product of two tensors $\mathcal{B} \in \mathbb{R}^{P_1 \times \dots \times P_l \times Q_1 \times \dots \times Q_d}$ and $\mathcal{X} \in \mathbb{R}^{P_1 \times \dots \times P_l}$ is denoted as $\mathcal{X} * \mathcal{B} \in \mathbb{R}^{Q_1 \times \dots \times Q_d}$ and is defined as

$$(\mathcal{X} * \mathcal{B})_{q_1 \dots q_d} = \sum_{p_1, \dots, p_l} \mathcal{X}_{p_1, \dots, p_l} \mathcal{B}_{p_1, \dots, p_l, q_1, \dots, q_d}.$$

3 Multiple Tensor-on-Tensor Regression Framework

In this section, we introduce the multiple tensor-on-tensor (MTOT) framework as an approach for integrating multiple sources of data with different dimensions and forms to model a process. Assume a set of training data of size M is available and includes response tensors $\mathcal{Y}_i \in \mathbb{R}^{Q_1 \times \dots \times Q_d}$ ($i = 1, \dots, M$) and input tensors $\mathcal{X}_{ji} \in \mathbb{R}^{P_{j1} \times \dots \times P_{jl}}$ ($i = 1, \dots, M; j = 1, \dots, p$), where p is the number of inputs. The goal of MTOT is to model the relationship between the input tensors and the response using the linear form

$$\mathcal{Y}_i = \sum_{j=1}^p \mathcal{X}_{ji} * \mathcal{B}_j + \mathcal{E}_i, \quad i = 1, \dots, M, \quad (1)$$

where $\mathcal{B}_j \in \mathbb{R}^{P_{j1} \times \dots \times P_{jl_j} \times Q_1 \times \dots \times Q_d}$ is the model parameter to be estimated and \mathcal{E}_i is an error tensor whose elements are from a random process. To achieve a more compact representation of the model (1), we can combine tensors \mathcal{Y}_i , \mathcal{X}_{ji} , and \mathcal{E}_i ($i = 1, \dots, M$) into one-mode larger tensors $\mathcal{Y} \in \mathbb{R}^{M \times Q_1 \times \dots \times Q_d}$, $\mathcal{X}_j \in \mathbb{R}^{M \times P_{j1} \times P_{j2} \times \dots \times P_{jl_j}}$ ($j = 1, 2, \dots, p$), and $\mathcal{E} \in \mathbb{R}^{M \times Q_1 \times \dots \times Q_d}$ and write

$$\mathcal{Y} = \sum_{j=1}^p \mathcal{X}_j * \mathcal{B}_j + \mathcal{E}. \quad (2)$$

The matricization of (2) gives

$$\mathbf{Y}_{(1)} = \sum_{j=1}^p \mathbf{X}_{j(1)} \mathbf{B}_j + \mathbf{E}_{(1)}, \quad (3)$$

where $\mathbf{Y}_{(1)}$ and $\mathbf{X}_{j(1)}$ are mode-1 unfolding of tensors \mathcal{Y} and \mathcal{X}_j , respectively, and the first mode corresponds to the sample mode. $\mathbf{B}_j \in \mathbb{R}^{P_j \times Q}$ is an unfold of tensor \mathcal{B}_j with $P_j = \prod_{k=1}^{l_j} P_{jk}$ and $Q = \prod_{k=1}^d Q_k$. It is intuitive that the parameters of (3) can be estimated by minimizing the mean squared loss function $L = \|\mathbf{Y}_{(1)} - \sum_{j=1}^p \mathbf{X}_{j(1)} \mathbf{B}_j\|_F^2$. However, this requires estimating $\sum_{j=1}^p \prod_{i=1}^{l_j} P_{ji} \prod_{k=1}^d Q_k$ parameters. For example, in the situation in which $p = 1$, minimizing the loss function gives a closed-form solution $\hat{\mathbf{B}} = \left(\mathbf{X}_{(1)}^T \mathbf{X}_{(1)} \right)^{-1} \mathbf{X}_{(1)}^T \mathbf{Y}_{(1)}$ that requires estimating $\prod_{i=1}^{l_1} P_i \prod_{j=1}^d Q_j$ parameters. Estimating such a large number of parameters is prone to severe overfitting and is often intractable. In reality, due to the structured correlation between \mathcal{X}_j and \mathcal{Y} , we can assume that the parameter \mathcal{B}_j lies in a much lower dimensional space and can be expanded using a set of basis matrices via a tensor product. That is, for each \mathcal{B}_j ($j = 1, \dots, p$), we can write

$$\mathcal{B}_j = \mathcal{C}_j \times_1 \mathbf{U}_{j1} \times_2 \mathbf{U}_{j2} \times_3 \dots \times_{l_j} \mathbf{U}_{jl_j} \times_{l_j+1} \mathbf{V}_1 \times_{l_j+2} \dots \times_{l_j+d} \mathbf{V}_d, \quad (4)$$

where $\mathcal{C}_j \in \mathbb{R}^{\tilde{P}_{j1} \times \dots \times \tilde{P}_{jl_j} \times \tilde{Q}_1 \times \dots \times \tilde{Q}_d}$ is a core tensor with $\tilde{P}_{ji} \ll P_{ji}$ ($j = 1, \dots, p; i = 1, \dots, l_j$) and $\tilde{Q}_i \ll Q_i$ ($i = 1, \dots, d$); $\{\mathbf{U}_{ji} : j = 1, \dots, p; i = 1, \dots, l_j\}$ is a set of bases that spans the j^{th} input space; and $\{\mathbf{V}_i : i = 1, \dots, d\}$ is a set of bases that spans the output space. With this low-dimensional representation, the estimation of \mathcal{B}_j reduces to learning the core tensor \mathcal{C}_j and the basis matrices \mathbf{U}_{ji} and \mathbf{V}_i . In this paper, we allow \mathbf{U}_{ji} to be learned directly from the input spaces. Two important choices of \mathbf{U}_{ji} are truncated identity matrices (i.e., no transformation on the inputs) or

the bases obtained from Tucker decomposition of the input tensor \mathcal{X}_j , i.e.,

$$\{\mathcal{D}_j, \mathbf{U}_{j1}, \dots, \mathbf{U}_{jl_j}\} = \arg \min_{\mathcal{D}_j, \{\mathbf{U}_{ji}\}} \|\mathcal{X}_j - \mathcal{D}_j \times_1 \mathbf{U}_{j1} \times \dots \times_{l_j} \mathbf{U}_{jl}\|_F^2.$$

In a special case that an input tensor is a matrix, the bases are the principle components (PCs) of that input if one uses Tucker decomposition. Allowing \mathbf{U}_{ji} ($j = 1, \dots, p; i = 1, \dots, l_j$) to be selected is reasonable because \mathcal{X}_j is an independent variable, and its basis matrices can be obtained separately from the output space. Furthermore, learning the core tensors \mathcal{C}_j ($j = 1, \dots, p$) and the bases \mathbf{V}_i ($i = 1, \dots, d$) provides a sufficient degree of freedom to learn \mathcal{B}_j . Next, we iteratively estimate the core tensors \mathcal{C}_j and the basis matrices \mathbf{V}_i by solving the following optimization problem:

$$\begin{aligned} \{\mathcal{C}_j, \mathbf{V}_1, \dots, \mathbf{V}_d\} &= \arg \min \left\| \mathbf{Y}_{(1)} - \sum_{j=1}^p \mathbf{X}_{j(1)} \mathbf{B}_j \right\|_F^2, \text{ s.t.} \\ \mathcal{B}_j &= \mathcal{C}_j \times_1 \mathbf{U}_{j1} \times_2 \mathbf{U}_{j2} \times_3 \dots \times_{l_j} \mathbf{U}_{jl_j} \times_{l_j+1} \mathbf{V}_1 \times_{l_j+2} \dots \times_{l_j+d} \mathbf{V}_d, \\ \mathbf{V}_i^T \mathbf{V}_i &= \mathbf{I}_{\tilde{Q}_i} \quad (i = 1, \dots, d), \end{aligned} \tag{5}$$

where $\mathbf{I}_{\tilde{Q}_i}$ is a $\tilde{Q}_i \times \tilde{Q}_i$ identity matrix. The first constraint ensures that the tensor of parameters is low-rank, and the orthogonality constraint $\mathbf{V}_i^T \mathbf{V}_i = \mathbf{I}_{\tilde{Q}_i}$ ensures the uniqueness of both the bases and the core tensors when the problem is identifiable. In general, the problem of estimating functional data through a set of functions may not be identifiable under some conditions. That is, assuming $p = 1$, one can find $\mathbf{B} \neq \bar{\mathbf{B}}$, such that $\mathbf{B}X = \bar{\mathbf{B}}X$, i.e., \mathbf{B} and $\bar{\mathbf{B}}$ both estimate same mean value for the output. He *et al.* (2000); Chiou *et al.* (2004); Lock (2017) discuss the identifiability problem in functional and tensor regression. Because the main purpose of this paper is to estimate and predict the output, we do not discuss the identifiability issue here, as learning any correct set of parameters $\{\mathbf{B}_k : k = 1, \dots, p\}$ will eventually lead to the same estimation of the output.

In order to solve (5), we combine the alternating least square (ALS) approach with the block coordinate decent (BCD) method (designated by ALS-BCD). The advantages of ALS algorithms that lead to their widespread use are conceptual simplicity, noise robustness, and computational efficiency (Sharan & Valiant, 2017). In tensor decomposition and regression, due to the non-convex nature of the problem, finding the global optimum is often intractable, and it is well-known that

the ALS algorithm also has no global convergence guarantee and may be trapped in a local optima (Kolda, 2006; Sharan & Valiant, 2017). However, ALS has shown great promise in the literature for solving tensor decomposition and regression applications with satisfying results. To be able to employ ALS-BCD, we first demonstrate Proposition 2:

Proposition 2. *When \mathbf{U}_{ki} ($k = 1, \dots, p; i = 1, 2, \dots, l_j$), \mathbf{V}_i ($i = 1, 2, \dots, d$), and \mathcal{C}_k ($k \neq j$) are known, a reshaped form of the core tensor \mathcal{C}_j can be estimated as*

$$\tilde{\mathcal{C}}_j = \mathcal{R}_j \times_1 (\mathbf{Z}_j^T \mathbf{Z}_j)^{-1} \mathbf{Z}_j^T \times_2 (\mathbf{V}_1^T \mathbf{V}_1)^{-1} \mathbf{V}_1^T \times_3 (\mathbf{V}_2^T \mathbf{V}_2)^{-1} \mathbf{V}_2^T \cdots \times_{d+1} (\mathbf{V}_d^T \mathbf{V}_d)^{-1} \mathbf{V}_d^T, \quad (6)$$

where $\mathbf{Z}_j = \mathbf{X}_{j(1)}(\mathbf{U}_{jl} \otimes \mathbf{U}_{jl-1} \otimes \cdots \otimes \mathbf{U}_{j1})$ and $\mathcal{R}_j = \mathcal{Y} - \sum_{i \neq j}^p \mathcal{B}_j * \mathcal{X}_j$. Note that $\tilde{\mathcal{C}}_j$ has fewer modes ($d + 1$) than the original core tensor \mathcal{C}_j in (4), but it can be transformed into \mathcal{C} by a simple reshape operation.

The simplified proof of this proposition is given in Appendix A. Furthermore, if \mathbf{V}_i s are orthogonal, the core tensor can be obtained efficiently by the tensor product as

$$\tilde{\mathcal{C}}_j = \mathcal{R}_j \times_1 (\mathbf{Z}_j^T \mathbf{Z}_j)^{-1} \mathbf{Z}_j^T \times_2 \mathbf{V}_1^T \times_3 \mathbf{V}_2^T \cdots \times_{d+1} \mathbf{V}_d^T.$$

Note that in the situations in which sparsity of the core tensor is of interest, one can include a lasso penalty over the core tensor, and use numerical algorithms (e.g., Iterative Shrinkage-Thresholding Algorithm (Beck & Teboulle, 2009)) to solve the problem. Furthermore, one can estimate the basis matrices \mathbf{V}_i as follows:

Proposition 3. *With known \mathcal{C}_j , \mathbf{U}_{ji} , and \mathbf{V}_k ($k \neq i$), we can solve \mathbf{V}_i by*

$$\mathbf{V}_i = \mathbf{R}\mathbf{W}^T,$$

where \mathbf{R} and \mathbf{W} are obtained from the singular value decomposition of $\mathbf{Y}_{(i)}\mathbf{S}^T$, where $\mathbf{S} = \sum_{j=1}^p \mathbf{S}_j$ and $\mathbf{S}_j = \tilde{\mathcal{C}}_{j(i)}(\mathbf{V}_d \otimes \cdots \otimes \mathbf{V}_{i+1} \otimes \mathbf{V}_{i-1} \cdots \otimes \mathbf{V}_1 \otimes \mathbf{Z}_j)^T$; and $\tilde{\mathcal{C}}_{j(i)}$ is the mode- i matricization of tensor $\tilde{\mathcal{C}}_j$. Note that \mathbf{R} is truncated.

The simplified proof of this proposition is shown in Appendix B. First note that we do not require calculation of the Kronecker product $\mathbf{V}_d \otimes \cdots \otimes \mathbf{V}_{i+1} \otimes \mathbf{V}_{i-1} \otimes \mathbf{V}_1 \otimes \mathbf{Z}$ explicitly to find

$\mathbf{Y}_{(i)}\mathbf{S}^T$. In real implementation, we can use Proposition 1 to calculate the complete matrix using tensor products efficiently. Second, unlike the principle component regression (PCR) in which the principle components of the output are learned independent of the inputs, the estimated basis matrices \mathbf{V}_i ($i = 1, \dots, d$) directly depend on the input tensors, ensuring correlation between the bases and inputs. By combining Propositions 2 and 3, Algorithm 1 summarizes the estimation procedure for multiple tensor-on-tensor regression. This algorithm, in fact, combines the block coordinate decent (BCD) algorithm with the ALS algorithm.

Algorithm 1 Estimation procedure for multiple tensor-on-tensor regression

- 1: Initialize \mathcal{C}_j for all j
 - 2: Estimate U_{j_i} using Tucker decomposition of \mathcal{X}_j for all i and j
 - 3: Initialize V_i for all i
 - 4: Compute B_j for all j and set $w_0 = \left\| Y_{(1)} - \sum_{j=1}^p X_{j(1)} B_j \right\|_F^2$
 - 5: **do**
 - 6: Estimate \mathcal{C}_j for all $j = 1 : p$ using Proposition 2
 - 7: Estimate V_i for all $i = 1 : d$ using Proposition 3
 - 8: Compute B_j for all j and set $w_k = \left\| Y_{(1)} - \sum_{j=1}^p X_{j(1)} B_j \right\|_F^2$
 - 9: **while** $|w_{k+1} - w_k| > \epsilon$
-

3.1 Selection of tuning parameters

The proposed approach requires the selection of the values \tilde{P}_{j_i} ($j = 1, 2, \dots, p; i = 1, 2, \dots, l_j$) and \tilde{Q}_k ($k = 1, \dots, d$). For simplicity and practicality, we assume that for each predictor \mathcal{X}_j and the response \mathcal{Y} , the rank is fixed, i.e., $\tilde{P}_{j_1} = \tilde{P}_{j_2} = \dots = \tilde{P}_{j_{l_j}} = \tilde{P}_j$ and $\tilde{Q}_k = \tilde{Q}$. As a result, we only need to select $p+1$ parameters. For this purpose, we use the k-fold cross-validation method on a $(p+1)$ -D grid of parameters $(\tilde{P}_1, \tilde{P}_2, \dots, \tilde{P}_p, \tilde{Q})$ and find the tuple of parameters that minimizes the mean squared error. As a result, we should define a grid over the rank values. This is achieved as following: First, we unfold each tensor \mathcal{X}_j ($j = 1, 2, \dots, p$) and \mathcal{Y} along their first mode. Next, we find the rank of each unfolded matrix, denoted as $R_{x_1}, R_{x_2}, \dots, R_{x_p}$ and R_y . Then, for each \mathcal{X}_j ($j = 1, 2, \dots, p$) and \mathcal{Y} , we select the tuning parameters from $\mathcal{P}_j = \left\{ 1, \left\lceil \frac{R_{x_j}}{2^{\log_2 R_{x_j} - 1}} \right\rceil, \dots, \left\lceil \frac{R_{x_j}}{2^2} \right\rceil, \left\lceil \frac{R_{x_j}}{2} \right\rceil, R_{x_j} \right\}$ and $\mathcal{Q} = \left\{ 1, \left\lceil \frac{R_y}{2^{\log_2 R_y - 1}} \right\rceil, \dots, \left\lceil \frac{R_y}{2^2} \right\rceil, \left\lceil \frac{R_y}{2} \right\rceil, R_y \right\}$. Next, for each tuple $(\tilde{P}_1, \tilde{P}_2, \dots, \tilde{P}_p, \tilde{Q}) \in \mathcal{P}_1 \times \mathcal{P}_2 \times \dots \times \mathcal{P}_p \times \mathcal{Q}$, we calculate the average sum square error (RSS) and take the one that minimizes the RSS. For all studies in the next sections, we perform five-fold CV.

4 Performance Evaluation Using Simulation

This section contains two parts. In the first part, we only consider curve-on-curve regression and compare our proposed method to the function-on-function regression approach proposed by Luo & Qi (2017), designated as *sigComp*. The reason we compare our approach to sigComp is that sigComp can handle multiple functional inputs (curves) and learn the basis functions similar to our approach. In the second part, we conduct a set of simulation studies to evaluate the performance of the proposed method when the inputs or outputs are in the form of images, structured point clouds, or curves with jumps. In this part, we compare the proposed method with two benchmarks: 1) The first benchmark is the TOT approach proposed by Lock (2017), which can roughly be viewed as a general form of sigComp. Because this approach can only handle a single input tensor, when multiple inputs exist we perform a transformation to merge the inputs into one single tensor. 2) The second benchmark is based on principle component regression (PCR) similar to a benchmark considered in (Fan *et al.*, 2014). In this approach, we first matricize all the input and output tensors, then perform principle component analysis to reduce the dimension of the problem by computing the PCA scores of the first few principle components that explain at least v percent of the variation in the data. Next, we perform linear regression between the low-dimensional PC score of both inputs and output. More formally, let $\mathbf{X}_{j(1)} \in \mathbb{R}^{M \times P_j}$ and $\mathbf{Y}_{(1)} \in \mathbb{R}^{M \times Q}$ denote the mode-1 matricization of the inputs and output, and $\mathbf{X} = [\mathbf{X}_{1(1)}, \mathbf{X}_{2(1)}, \dots, \mathbf{X}_{p(1)}]$ be a concatenation of all the input matrices. We first compute the first G_x and G_y principle components of \mathbf{X} and the response $\mathbf{Y}_{(1)}$. Next, the PC scores of the input \mathbf{X} are calculated (a matrix in $\mathbb{R}^{M \times G_x}$) and are used to predict the matrix of the scores of the response function (a matrix in $\mathbb{R}^{M \times G_y}$). Then, given the PC scores of the new inputs, we use the fitted regression model to predict the response scores. Finally, we multiply the predicted response scores by the G_y principle components to obtain the original responses. The number of principle components G_x and G_y can be identified through a cross-validation procedure. In this paper, instead of cross-validating over G_x and G_y directly, we perform CV over the percentage of variation the PCs explain, i.e., v . For this purpose, we take the value of v from $\{85\%, 90\%, 95\%, 99\%, 99.5\%\}$ and take the v that minimizes the CV error. The standardized mean square prediction error (SMSPE) is used as a performance measure to compare the proposed method with the benchmarks. The SMSPE is defined as $SMSP E = \frac{\|\mathcal{Y} - \hat{\mathcal{Y}}\|_F^2}{\|\mathcal{Y}\|_F^2}$.

4.1 Simulation studies for curve-on-curve regression

In this simulation, we consider multiple functional (curve) predictors and multiple scalar predictors similar to the simulation study in (Luo & Qi, 2017). We first randomly generate $(\mathbf{B}_1, \mathbf{B}_2, \dots, \mathbf{B}_p)$ as follows:

$$\mathbf{B}_i(s, t) = \frac{1}{p^2} [\gamma_{1i}(t) \psi_{1i}(s) + \gamma_{2i}(t) \psi_{2i}(s) + \gamma_{3i}(t) \psi_{3i}(s)],$$

where $\gamma_{ki}(t)$ and $\psi_{ki}(s)$ ($k = 1, 2, 3; i = 1, \dots, p$) are Gaussian processes with covariance function $\Sigma_1(z, z') = \left(1 + 20|z - z'| + \frac{1}{3}(20|z - z'|)^2\right) e^{-20|z - z'|}$. Next, we generate $p = 1, 3, 6$, functional predictors using the following procedure: Let \mathbf{S} be a $p \times p$ matrix with the $(i, j)^{th}$ element equal to $\rho_c = 0, 0.5$ for $i \neq j$ and equal to one for diagonal elements. Next, we decompose $\mathbf{S} = \mathbf{\Delta} \mathbf{\Delta}^T$, where $\mathbf{\Delta}$ is a $p \times p$ matrix and generate a set of curves w_1, w_2, \dots, w_p using a Gaussian process with covariance function $\Sigma_2(z, z') = e^{-(2|z - z'|)^2}$. Finally, we generate the predictors at any given point s as

$$(x_1(s), \dots, x_p(s)) = (w_1(s), w_2(s), \dots, w_p(s)) \mathbf{\Delta}^T.$$

With this formulation, each curve of $x_1(s), \dots, x_p(s)$ is a Gaussian process with covariance function $\Sigma_2(s, s')$, and for each s , the vector $(x_1(s), \dots, x_p(s))$ is a multivariate normal distribution with covariance \mathbf{S} . When $\rho_c = 0$, this vector becomes an independent vector of normally distributed variables. Figure 2 illustrates examples of the predictors when $p = 3$ for $\rho_c = 0, 0.5$. We also generate the scalar predictors (u_1, \dots, u_5) from a multivariate normal distribution with mean vector zero and the covariance matrix with diagonal elements equal to 1 and off-diagonal elements equal to 0.5. The coefficients of the scalar variables denoted by $\alpha_i(t)$ ($i = 1, \dots, 5$) are generated from a Gaussian process with covariance function $\Sigma(t, t') = e^{\{-5|t - t'|\}^2}$. Finally, we generate the response curves as

$$y(t) = \sum_{i=1}^5 \alpha_i(t) u_i + \sum_{i=1}^p \int \mathbf{B}_i(s, t) x_i(s) ds + \epsilon(t),$$

where $\epsilon(t)$ is generated from a normal distribution with zero mean and $\sigma^2 = 0.1$. We generate all of the input and output curves over $0 < s < 2$ and $0 < t < 1$ and take the samples over an equidistant grid of size 100.

For each combination of (p, ρ_c) , we compare the performance of the proposed method with the methods in (Luo & Qi, 2017) based on the mean square prediction error (MSPE) and the mean

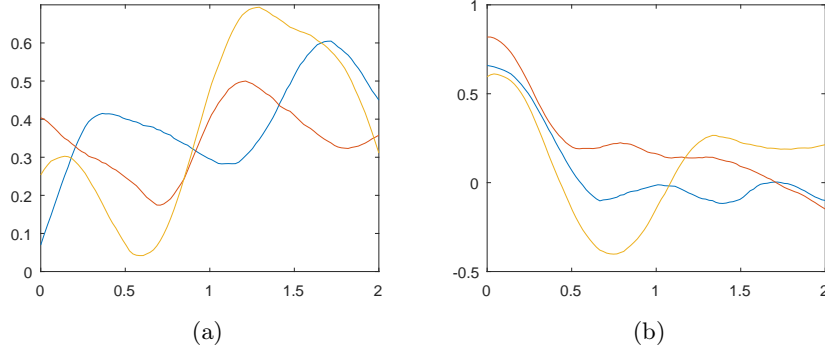


Figure 2: Example of the predictors when (a) $p = 3, \rho_c = 0$ and (b) $p = 3, \rho_c = 0.5$.

square estimation error (MSEE). We do not compare our approach to PCR in this simulation because sigComp has already demonstrated superiority over PCR in simulation studies in (Luo & Qi, 2017). We implement the sigComp benchmark method using the R package *FRegSigCom* in which we use 50 spline bases for both the inputs and output and default convergence tolerance. To calculate the MSPE and MSEE, we first generate a sample data of size $M_{train} = 400$ that is used to learn the model parameters. Next, we generate a testing sample of size $M_{test} = 100$ and calculate MSPE as

$$MSPE = \frac{1}{M_{test}} \sum_{j=1}^{M_{test}} \left(\frac{1}{100} \sum_{i=1}^{100} (y_j^{test}(t_i) - \hat{y}_j^{test}(t_i))^2 \right)$$

and

$$MSEE = \frac{1}{M_{test}} \sum_{j=1}^{M_{test}} \frac{1}{100} \sum_{i=1}^{100} (y_j^{test}(t_i) - \epsilon(t_i) - \hat{y}_j(t_i))^2.$$

We repeat this procedure 50 times to find the means and standard deviations of the MSPE and MSEE for each method. Table 1 reports the results at different values of ρ_c and different numbers of predictors, p . As reported, our proposed approach is superior to the sigComp method in terms of MSPE and MSEE for $p = 1, 3$. For example, when $p = 3$ and $\rho_c = 0.5$, the average MSPE and MSEE of the sigComp are 0.2052 and 0.1048, which are much larger than the corresponding values (0.1282 and 0.0286) achieved by MTOT. However, the performance of sigComp is comparable or even slightly better than MTOT for $p = 6$. For example, when $p = 6$ and $\rho_c = 0.5$, the average MSPE is 0.1104 for sigComp and 0.1121 for MTOT. The reason that sigComp performs slightly better for a larger p is that it imposes sparsity when estimating the parameters, thus reducing the

Table 1: Comparison between the proposed method and the sigComp method proposed by Luo & Qi (2017).

p	ρ_c	<i>sigComp</i>		<i>MTOT</i>	
		MSPE	MSEE	MSPE	MSEE
1	0	0.7155 (0.0413)	0.6139 (0.0414)	0.1039 (0.00130)	0.0025 (0.0001)
3	0	0.2052 (0.0089)	0.1048 (0.0087)	0.1282 (0.0064)	0.0286 (0.0061)
	0.5	0.2086 (0.0105)	0.0934 (0.0106)	0.1159 (0.0034)	0.0140 (0.0029)
6	0	0.1052 (0.0011)	0.0055 (0.0011)	0.1051 (0.0010)	0.0053 (0.0003)
	0.5	0.1104 (0.0018)	0.0106 (0.008)	0.1121 (0.0035)	0.0141 (0.0043)

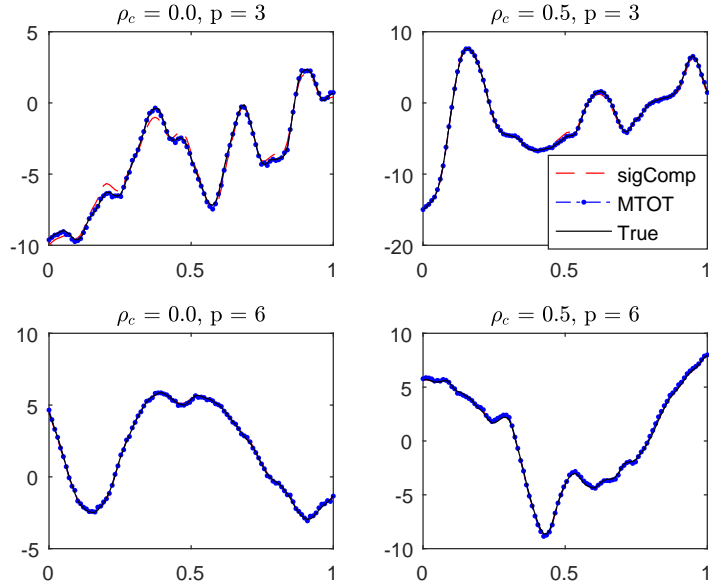


Figure 3: Prediction examples of sigComp and MTOT for different p and ρ_c .

chance of overfitting. Figure 3 illustrates prediction examples obtained by each method, along with the true curve for different p . As illustrated both of the approaches produce accurate predictions for $p = 6$.

4.2 Simulation studies for image/ structured point-cloud or non-smooth output

Case I–Waveform surface simulation: We simulate waveform surfaces \mathcal{Y}_i based on two input tensors, $\mathcal{X}_{1i} \in \mathbb{R}^{P_{11} \times P_{12} \times \dots \times P_{1l_1}}$ and $\mathcal{X}_{2i} \in \mathbb{R}^{P_{21} \times P_{22} \times \dots \times P_{2l_2}}$ ($i = 1, \dots, M$), where M is the number of samples.

To generate the input tensors, we define $x_{kmj} = \frac{j}{P_{km}}$ ($k = 1, 2; m = 1, \dots, l_k; j = 1, \dots, P_{km}$). Then, we set $\mathbf{U}_{km} = [\mathbf{u}_{km1}, \mathbf{u}_{km2}, \dots, \mathbf{u}_{kmP_{km}}]$ ($k = 1, 2; m = 1, \dots, l_k$), where

$$\mathbf{u}_{kmt} = \begin{cases} [\cos(2\pi t x_{km1}), \dots, \cos(2\pi t x_{kmP_{km}})]^T & \text{if } t \text{ is odd} \\ [\sin(2\pi t x_{km1}), \dots, \sin(2\pi t x_{kmP_{km}})]^T & \text{if } t \text{ is even.} \end{cases}$$

Next, we randomly simulate elements of a core tensor \mathcal{D}_{ki} from a standard normal distribution. Then, we generate an input sample using the following model:

$$\mathcal{X}_{ki} = \mathcal{D}_{ki} \times_1 \mathbf{U}_{k1} \times_2 \dots \times_{l_k} \mathbf{U}_{kl_k} \quad (k = 1, 2; i = 1, \dots, M).$$

To generate a response tensor, we first simulate the elements of a core tensor \mathcal{C}_k from a standard normal distribution. Moreover, we set $\mathbf{V}_m = [\mathbf{v}_{m1}, \mathbf{v}_{m2}, \dots, \mathbf{v}_{mQ_m}]$ ($m = 1, \dots, d$), where

$$\mathbf{v}_{mt} = \begin{cases} [\cos(2\pi t y_{m1}), \dots, \cos(2\pi t y_{mQ_m})]^T & \text{if } t \text{ is odd} \\ [\sin(2\pi t y_{m1}), \dots, \sin(2\pi t y_{mQ_m})]^T & \text{if } t \text{ is even} \end{cases}$$

and $y_{mj} = \frac{j}{Q_m}$. Next, we define the parameter tensors \mathcal{B}_k using the following expansion:

$$\mathcal{B}_k = \mathcal{C}_k \times_1 \mathbf{U}_{k1} \times_2 \dots \times_{l_k} \mathbf{U}_{kl_k} \times_{l_k+1} \mathbf{V}_1 \times \dots \times_{l_k+d} \mathbf{V}_d.$$

Finally, we simulate a response tensor as

$$\mathcal{Y}_i = \sum_{k=1}^2 \mathcal{X}_{ki} * \mathcal{B}_k + \mathcal{E}_i,$$

where \mathcal{E}_i is the error tensor whose elements are sampled from a normal distribution $\mathcal{N}(0, \sigma^2)$. For simulation purposes, we assume $\mathcal{X}_{1i} \in \mathbb{R}^{60}$, $\mathcal{X}_{2i} \in \mathbb{R}^{50 \times 50}$, and $\mathcal{Y}_i = \mathbb{R}^{60 \times 40}$. That is, we generate a response based on a profile and an image signal. Furthermore, we set $R_1 = 2$, $R_2 = 3$, and $R = 3$. This implies that $\mathcal{C}_1 \in \mathbb{R}^{2 \times 3 \times 3}$ and $\mathcal{C}_2 \in \mathbb{R}^{3 \times 3 \times 3}$. Figure 4a illustrates examples of generated response surfaces. For this simulation study, we first generate a set of $M = 200$ data points. Then, we randomly divide the data into a set of size 160 for training and a set of size 40 for testing.

We perform CV and train the model using the training set, then calculate the SMSPE for the proposed method and benchmarks based on the testing data. We repeat this procedure 50 times to capture the variance of the SMSPE. In order to prepare data for the TOT approach, three steps are performed: First, because the dimension of the curve inputs (1×60) and the image inputs (50×50) do not match, we randomly select 50 points out of 60 to reduce the curve dimension to 50. Second, we replicate each curve 50 times to generate 50×50 images. Third, for each sample, we merge the image constructed from the curve and the image input to construct a tensor of size $50 \times 50 \times 2$. Combining all of the samples, we obtain an input tensor of size $M \times 50 \times 50 \times 2$, where M is the sample size.

Case II–Truncated cone simulation: We simulate a truncated cone based on a set of scalars and simple profile data in a 3D cylindrical coordinate system (r, ϕ, z) , where $\phi \in [0, 2\pi]$ and $z \in [0, 1]$. We first generate an equidistant grid of $I_1 \times I_2$ over the (ϕ, z) space by setting $\phi_i = \frac{2\pi i}{I_1}$ ($i = 1, \dots, I_1$) and $z_j = \frac{j}{I_2}$ ($j = 1, \dots, I_2$). Specifically, we set $I_1 = I_2 = 200$. Next, we simulate the truncated cone over the grid by

$$r(\phi, z) = \frac{r_0 + z \tan \theta}{\sqrt{1 - e^2 \cos^2 \phi}} + c(z^2 - z) + \epsilon(\phi, z), \quad (7)$$

where r_0 is the radii of the upper circle of the truncated cone, θ is the angle of the cone, e is the eccentricity of the top and bottom surfaces, c is the side curvatures of the truncated cone, and $\epsilon(\phi, z)$ is process noise simulated from $\mathcal{N}(0, \sigma^2)$. Figure 4b illustrates examples of generated truncated cones. We assume that the parameters of the truncated cone are specific features obtained from a scalar and three simple profile data. In particular, we assume that the scalar predictor is $x_{1i} = r_{0i}$ and the profile predictors are $x_{2i}(z) = z \tan \theta$, $x_{3i}(\phi) = e^2 \cos^2 \phi$, and $x_{4i}(z) = c(z^2 - z)$; $i = 1, \dots, M$. That is, the inputs are one scalar and three profiles. We simulate these profiles for training purposes by setting the parameters as follows: We set $r_0 \in \{1.1, 1.3, 1.5\}$, $\theta \in \{0, \frac{\pi}{8}, \frac{\pi}{4}\}$, $e \in \{0, 0.3, 0.5\}$, $c \in \{-1, 0, 1\}$, and consider a full factorial design to generate 81 samples. That is, for each combination of parameters (e.g., $\{1.1, 0, 0.3, -1\}$), we generate a sample containing one scalar value and three profiles. We represent each of the inputs by a matrix (a tensor of order 2) to obtain four input matrices X_1, X_2, X_3 , and X_4 , where $X_1 \in \mathbb{R}^{81 \times 1}$ and $X_i \in \mathbb{R}^{81 \times 200}$ ($i = 2, 3, 4$).

Finally, we generate the testing data by sampling the truncated cone parameters as follows: We assume $r \sim U(1.1, 1.5)$, $\theta \sim U(0, \frac{\pi}{4})$, $e \sim U(0, 0.5)$, and $c \sim U(-1, 1)$, where $U(a, b)$ denotes a uniform distribution over the interval $[a, b]$, and sample each parameter from its corresponding distribution. In this simulation, we first train the model using the generated training data. Next, we generate a set of 1000 testing data. We predict the truncated cone based on the input values in the testing data and calculate the SMSPE for each predicted cone. In order to prepare the data for TOT, we first replicate the column of X_1 to generate a matrix of size 81×200 , then merge this matrix with the other three matrices to construct an input tensor of size $81 \times 4 \times 200$. This tensor is used as an input in the TOT.

Case III—Curve response with jump simulation: We simulate a response function with jump using a group of B-spline bases. Let $t_i = \frac{i}{I}$ with $i = 0, 1, \dots, I$ and $I = 200$ and let $B_1 \in \mathbb{R}^{I \times 5}$ and $B_2 \in \mathbb{R}^{I \times 51}$ be two matrices of fourth-order B-spline bases obtained by one and 47 knots over $[0, 1]$. We generate a response profile by combining these two bases as follows:

$$y_j(t_i) = B_1(t_i) x_{1j} + B_2(t_i) x_{2j} + e(t_i),$$

where $B_1(t_i)$ and $B_2(t_i)$ are basis evaluations at the point t_i , and $e(t_i)$ is a random error simulated from $\mathcal{N}(0, \sigma^2)$. The input vector x_{1j} is dense, and its elements are generated from a uniform distribution over $[0, 1]$. x_{2j} is a sparse vector with five consecutive elements equal to one and the rest equal to zero. The location of five consecutive elements is selected at random. Figure 4c illustrates examples of response functions. For this simulation study, we first generate a set of $M = 500$ data points, i.e., $\{(y_j, x_{1j}, x_{2j})\}_{j=1}^M$. Then, we randomly divide the data into a set of size 400 for training and a set of size 100 for testing. We perform CV and train the model using the training data set. Next, we calculate the SMSPE for the proposed method and the benchmark based on the testing data. We repeat this procedure 50 times to capture the variance of the SMSPE.

In each case, we compare the proposed method with benchmarks based on the SMSPE calculated at different levels of noise σ . Tables 2, 3, and 4 report the average and standard deviation of SMSPE (or its logarithm), along with the average running time of each algorithm for the simulation cases I, II, and III, respectively. In Table 3, we report the average and standard deviation of the

logarithm of the SMSPE for better comparison of the values. Please notice that the SMSPE is a standardized error and should not directly be compared to the variance. In all cases, the MTOT has the smallest prediction errors, reflecting the advantage of our method in terms of prediction. Furthermore, with the increase in σ , all methods illustrate a larger SMSPE in all cases. In the first case, the TOT illustrates a prediction performance comparable to our method at a cost of a much longer running time. For example, when $\sigma = 0.2$, TOT requires about 147.33 seconds to reach the SMSPE of 0.0170, obtained in 1.05 seconds by MTOT. The performance of both PCR and TOT are significantly worse than MTOT in the second case. The inferior performance of TOT is due to both its restriction on selecting the same rank for both the input and output and the fact that the CP decomposition it uses does not consider the correlation between multiple modes.

In the third case, the prediction performances of all three methods are comparable, indicating that all three are capable of predicting a functional output with discontinuity. However, our approach shows slightly smaller prediction errors. Although the running time of the PCR is significantly lower than the other two approaches, MTOT running time is reasonable and within two-tenths of a second. The TOT shows slightly larger prediction error in all cases with much longer running time, making this approach less appealing. Recall that in this simulation, we used B-spline bases as the coefficients of the input to generate the output curve. Figure 5a illustrates the plot of the columns of the learned coefficient matrix that corresponds to B_1 . As can be seen, the learned bases are very similar to B-spline bases used originally as the coefficients. Figure 5b illustrates some of the columns of the learned parameters that correspond to B_2 . Unlike the first set of parameters, these parameters are slightly different from the B-spline bases that are originally used for data generation purposes. This is due to the identifiability issue. Our approach imposes an orthogonality restriction that may generate a set of parameters (when the identifiability issue exists) different from the parameters from which the data is originally generated, but that can still produce accurate predictions in terms of the mean value.

5 Case Study

In semiconductor manufacturing, patterns are printed layer by layer over a wafer in a sequence of deposition, etching, and lithographic processes to manufacture transistors (Nishi & Doering, 2000).

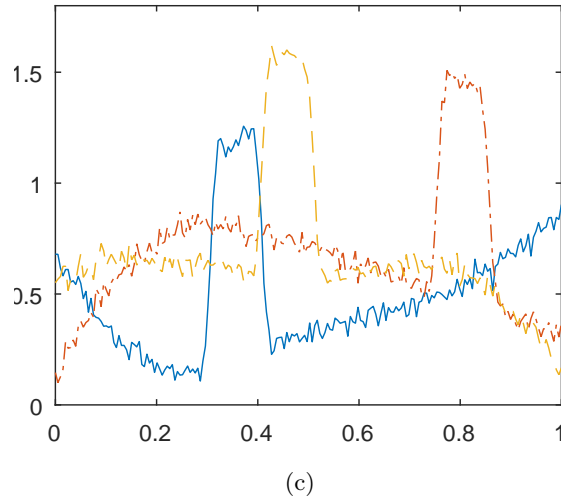
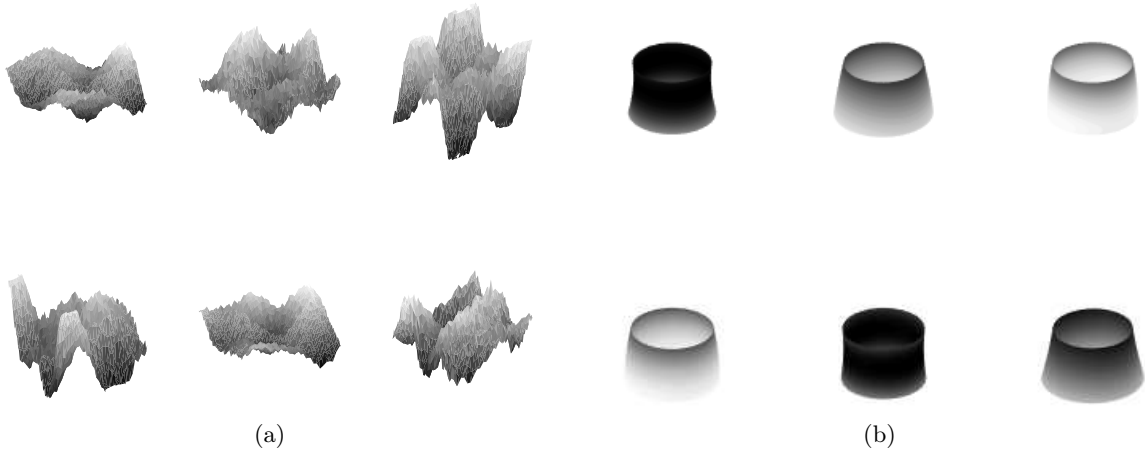


Figure 4: Examples of generated output for the simulation study (a) case I-waveform surface, (b) case II-truncated cone, and (c) response function with jump.

Table 2: Comparison between the proposed method (MTOT) and the benchmarks in case I with the waveform response. The TOT requires a much larger running time to achieve the same level of prediction error as the MTOT.

σ	<i>PCR</i>		<i>TOT</i>		<i>MTOT</i>	
	SMSPE	Time (sec)	SMSPE	Time (sec)	SMSPE	Time (sec)
0.1	0.0057 (0.0015)	0.03 (0.00)	0.0046 (0.0011)	154.98 (17.94)	0.0044 (0.0011)	1.05 (0.03)
0.2	0.0199 (0.0045)	0.04 (0.00)	0.0170 (0.0039)	147.33 (2.47)	0.0170 (0.0040)	1.05 (0.01)
0.3	0.0455 (0.0097)	0.04 (0.00)	0.0399 (0.0086)	149.03 (1.36)	0.0395 (0.0086)	1.05 (0.02)
0.4	0.0773 (0.0233)	0.04 (0.00)	0.0678 (0.0135)	149.13 (0.96)	0.0673 (0.0212)	1.05 (0.03)
0.5	0.1186 (0.0222)	0.04 (0.00)	0.1036 (0.0231)	146.17 (0.95)	0.1032 (0.0203)	1.04 (0.01)
0.6	0.1670 (0.0327)	0.04 (0.00)	0.1456 (0.0309)	147.75 (1.81)	0.1454 (0.0299)	1.03 (0.01)

Table 3: Comparison between the proposed method and the benchmarks in case II with truncated cone. Due to the difference between the input and the output rank, the performance of the TOT is significantly worse than the MTOT. The PCR is very fast in estimation, but the prediction accuracy is not as appealing as the MTOT.

σ	<i>PCR</i>		<i>TOT</i>		<i>MTOT</i>	
	log(SMSPE)	Time (sec)	log(SMSPE)	Time (sec)	log(SMSPE)	Time (sec)
0.01	-5.555 (0.986)	0.05 (0.00)	-5.249 (1.326)	23.58 (5.93)	-8.095 (1.196)	3.82 (0.09)
0.02	-5.509 (0.937)	0.07 (0.00)	-5.197 (1.254)	27.94 (6.11)	-7.629 (0.869)	3.92 (0.10)
0.03	-5.441 (0.879)	0.08 (0.00)	-5.127 (1.175)	29.11 (8.46)	-7.215 (0.666)	3.93 (0.12)
0.04	-5.360 (0.819)	0.06 (0.00)	-5.048 (1.097)	33.61 (9.02)	-6.856 (0.537)	3.95 (0.14)
0.05	-5.269 (0.762)	0.07 (0.00)	-4.963 (1.023)	34.29 (14.55)	-6.543 (0.454)	3.99 (0.13)
0.06	-5.173 (0.710)	0.07 (0.00)	-4.875 (0.956)	37.43 (15.19)	-6.266 (0.402)	3.95 (0.14)

Table 4: Comparison between the proposed method and the benchmarks in case III with a non-smooth response. All three methods produce reasonable predictions. However, the MTOT performs slightly better than the benchmarks within a reasonable running time.

σ	<i>PCR</i>		<i>TOT</i>		<i>MTOT</i>	
	SMSPE	Time (sec)	SMSPE	Time (sec)	SMSPE	Time (sec)
0.1	0.0255 (0.0010)	0.02 (0.00)	0.0250 (0.0008)	17.67 (0.58)	0.0230 (0.0007)	0.26 (0.01)
0.15	0.0503 (0.0018)	0.03 (0.00)	0.0510 (0.0018)	17.27 (0.20)	0.0496 (0.0017)	0.25 (0.01)
0.2	0.0851 (0.0027)	0.04 (0.00)	0.0862 (0.0026)	17.25 (0.22)	0.0848 (0.0028)	0.25 (0.01)
0.25	0.1260 (0.0043)	0.05 (0.00)	0.1271 (0.0042)	16.01 (2.32)	0.1255 (0.0042)	0.27 (0.00)
0.3	0.1730 (0.0046)	0.05 (0.00)	0.1734 (0.0041)	16.33 (2.67)	0.1725 (0.0046)	0.27 (0.01)
0.35	0.2305 (0.0051)	0.05 (0.00)	0.2333 (0.0066)	16.69 (0.83)	0.2230 (0.0052)	0.27 (0.00)

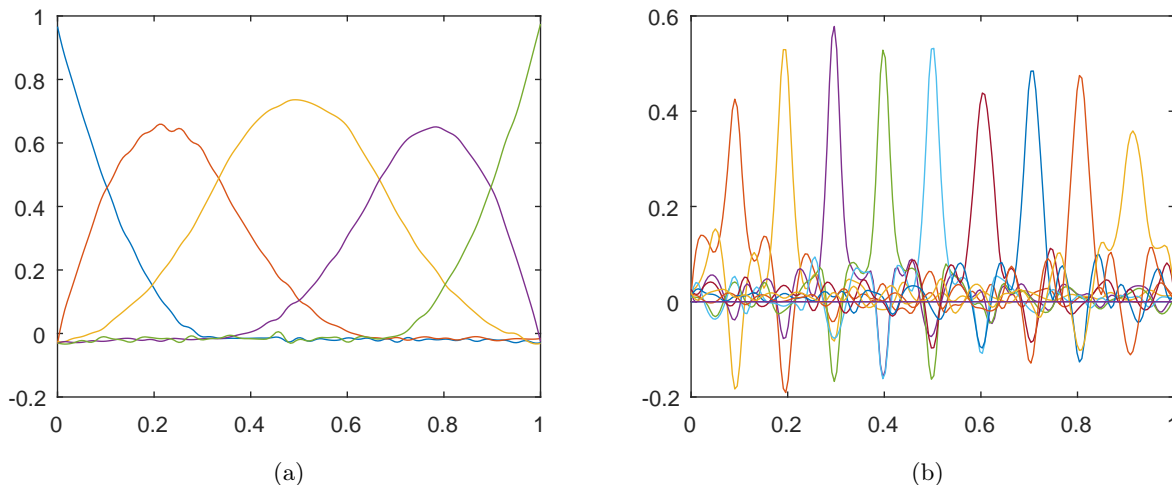


Figure 5: Examples of the learned parameters in simulation case III when $\sigma = 0$.

Many of these processes induce stress variations across the wafer, distorting/changing the wafer shape (Brunner *et al.*, 2013; Turner *et al.*, 2013). Figure 6 illustrates a simplified sequence of processes, causing the overlay error in the patterned wafers. In the first step, a layer is deposited over the wafer and exposed to rapid thermal annealing, causing a curvature in the free-state wafer. The wafer is then chucked flat and patterned in a lithographic process. Next, to generate a second layer pattern, a new layer is deposited, changing the wafer shape. Finally, in the lithography step, the flattened wafer is patterned. Because the wafer is flattened, the first pattern distance increases, but the new pattern is printed with the same distance L , generating a misalignment between patterns. The overlay error caused by lower order distortions can be corrected by most of the exposure tools. For this purpose, the alignment positions of several targets are measured and used to fit a linear overlay error model (Brunner *et al.*, 2013):

$$\begin{cases} \Delta x = T_x - \theta_x y + M_x x & \text{error in x coordinate} \\ \Delta y = T_y + \theta_y x + M_y y & \text{error in y coordinate,} \end{cases} \quad (8)$$

where x and y identify the position of the target point over the wafer, T_x and T_y are transition errors, θ_x and θ_y relate to rotation error, and M_x and M_y are isotropic magnification errors pertaining to the wafer size change or wafer expansion due to processing. The fitted model is then used to correct the overlay errors. This model, however, can only correct the overlay error induced by a uniform stress field and fails to compensate for overlay errors caused by high-order distortions (Brunner *et al.*, 2013). Therefore, developing a model that can relate the overlay error to higher order patterns in the wafer shape is essential for better overlay correction.

In this case study, we use our proposed method to predict the overlay error based on the wafer shape data. Such predictions can be fed forward to the exposure tools to result in a better correction strategy. In practice, the wafer shape is measured using a patterned wafer geometry (PWG) tool, and the overlay error is measured using standard optical methods (Brunner *et al.*, 2013). Both the wafer shapes and the overlay errors (in each coordinate, x or y) can be presented as image data. In this case study, we follow the procedure and results suggested and verified (through both experiments and finite element [FE] analysis) by Brunner *et al.* (2013) to generate surrogate data of overlay errors ($PIR(x, y)$) based on the wafer shape prior to two lithography steps ($w_1(x, y)$),

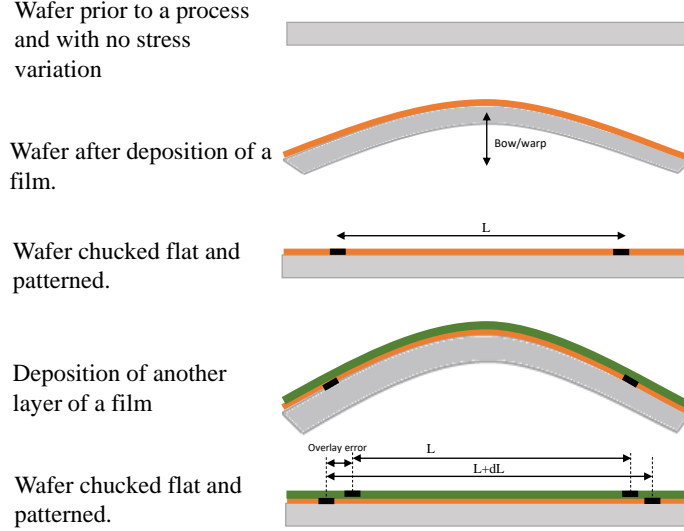


Figure 6: Process of a wafer, which causes shape variation and consequently overlay error.

$w_2(x, y)$). The data generation procedure is elaborated in Appendix C.

Based on the described procedure in Appendix C, we generate a set of 500 training observations, i.e., wafer shapes and overlay errors, $\{(w_{1i}(x, y), w_{2i}(x, y), PIR_i)\}_{i=1}^{M=500}$, and employ our proposed method to estimate the PIR_i based on $(w_{1i}(x, y), w_{2i}(x, y))$. Because in our simulated data $w_{1i}(x, y)$ remains fixed, we consider $w_i(x, y) = w_{2i}(x, y) - w_{1i}(x, y)$ as the predictor. We also generate 100 observations as the test dataset. The mean square prediction error obtained from the testing data is used as the performance criterion. We repeat the simulations 50 times and record the MSPE values. Because our proposed methodology assumes that the shapes are observed over a grid, we transform the data to the polar coordinate prior to modeling. In the polar space, each shape is observed over a grid of 100×200 (100 in the radial direction and 200 in the angular direction, with overall 20,000 pixels). Unfortunately, the TOT approach proposed by Lock (2017) failed to run with this size of images due to its high space complexity. Therefore, we only compared our approach with PCR. Figure 7 illustrates an example of the original and predicted corrected overlay error image, along with the prediction error. As illustrated, the proposed method predicted the original surface more accurately, with smaller errors across the wafer. Figure 8 illustrates the boxplots of the logarithm of the prediction mean square error calculated over the 50 replications in contrast with the benchmark. The results show that the proposed method is superior to the benchmark in prediction of the image. As an example, the average of $\log(\text{SMSE})$ over the replications is -8.33 for

the proposed method and -7.56 for the PCR approach.

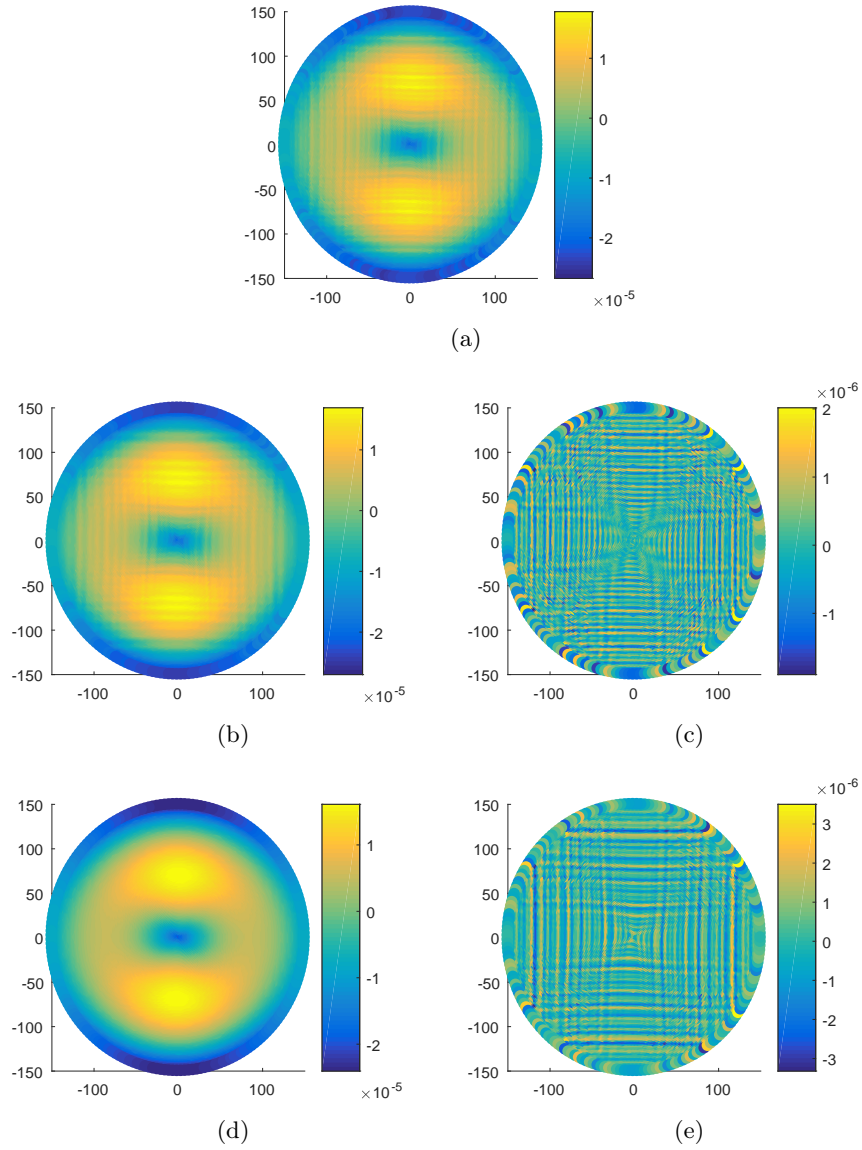


Figure 7: Example of (a) the x coordinate overlay error, (b) prediction of MTOT, (c) MTOT prediction error, (d) prediction of PCR, and (e) PCR prediction error.

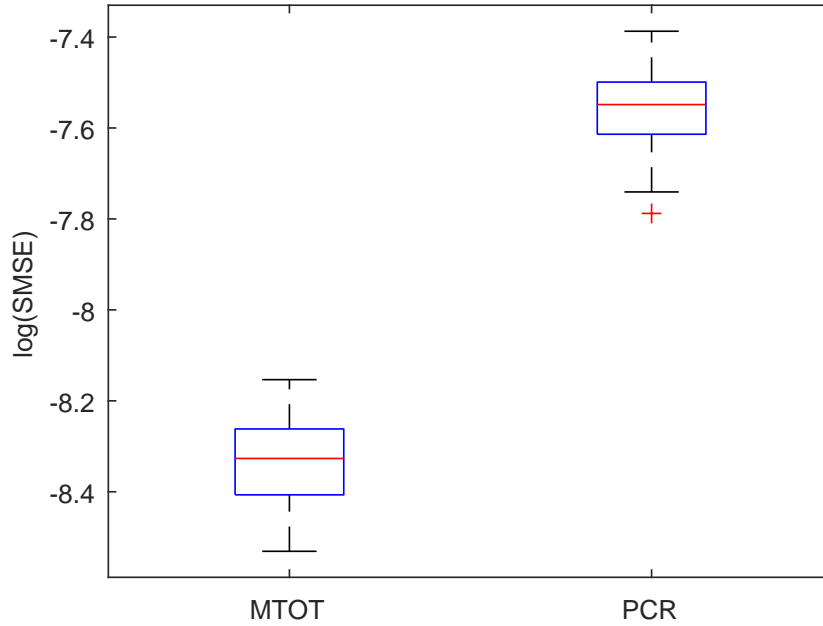


Figure 8: Logarithm of the prediction mean square error calculated for the test data over 50 replications. The proposed method illustrates significantly lower standard prediction error than the PCR approach.

6 Conclusion

This paper proposed a multiple tensor-on-tensor approach for modeling processes with a heterogeneous set of input variables and an output that can be measured by a scalar, curve, image, or point-cloud, etc. The proposed method represents each of the inputs as well as the output by tensors, and formulates a multiple linear regression model over these tensors. In order to estimate the parameters, a least square loss function is defined. In order to avoid overfitting, the proposed method decomposes the regression parameters through a set of basis matrices that spans the input and output spaces. Next, the basis matrices, along with their expansion coefficients, are learned by minimizing the loss function. The orthogonality condition is imposed over the output bases to assure identifiability and interpretability. To solve the minimization problem, first, a closed-form solution is derived for both the bases and their coefficients. Second, the block coordinate decent (BCD) approach combined with the ALS algorithm is applied. The proposed approach is capable of combining different forms of inputs (e.g., an image, a curve, and a scalar) to estimate an output

(e.g., a scalar, a curve, or an image, etc.) as demonstrated in first three simulation studies. For example, in the first and third simulation studies, we combined the scalar and profile inputs to estimate a profile and a point cloud, respectively; and in the second simulation study, a profile and an image are integrated to predict an image.

In order to evaluate the performance of the proposed method, we conducted four simulation studies and a case study. In our first simulation study, we compared our proposed method with the function-on-function approach proposed by Luo & Qi (2017). This simulation considered scalar and curve inputs since the benchmark can only handle those form of data. Next, we performed three other simulations to evaluate the performance of the proposed method when the inputs or outputs are images or point clouds. In these simulation studies, the proposed approach was compared with principle component regression (PCR) and tensor-on-tensor (TOT) regression, and showed superior performance in terms of mean squared prediction error. We also evaluated our proposed method using a set of surrogate data generated according to the manufacturing process of semiconductors. We simulated the shape and overlay errors for several wafers and applied the proposed method to estimate the overlay errors based on the wafer shapes measured prior to the lithography steps. Results showed that the proposed method performed significantly better than the PCR in predicting the overlay errors.

As a future work, including penalties such as lasso for sparsity and group lasso for variable selection and imposing roughness penalties over the basis matrices may improve the prediction results and can be further studied.

Appendix A: Proof of Proposition 2

For simplicity, we assume only one input tensor exists. Then, we can solve \mathcal{C} by

$$\begin{aligned}
\operatorname{argmin}_{\mathcal{C}} \|Y_{(1)} - X_{(1)}B\|_F^2 &= \|Y_{(1)} - X_{(1)}(U_l \otimes U_{l-1} \otimes \cdots \otimes U_1)C(V_d \otimes \cdots \otimes V_1)^T\|_F^2 \\
&= \|\operatorname{vec}(Y_{(1)}) - \operatorname{vec}(X_{(1)}(U_l \otimes U_{l-1} \otimes \cdots \otimes U_1)C(V_d \otimes \cdots \otimes V_1)^T)\|_2^2 \\
&= \|\operatorname{vec}(Y_{(1)}) - \operatorname{vec}(ZC(V_d \otimes \cdots \otimes V_1)^T)\|_2^2 \\
&= \|\operatorname{vec}(Y_{(1)}) - (V_d \otimes \cdots \otimes V_1 \otimes Z)\operatorname{vec}(C)\|_2^2,
\end{aligned}$$

where $vec(X)$ stacks the columns of matrix X on top of each other. This is a simple least square regression that gives a closed-form solution as in (6) after applying Proposition 1 to convert Kronecker products to tensor products.

Appendix B: Proof of Proposition 3

Again assuming a single input tensor, let us define $\tilde{Y} = (V_d \otimes \dots \otimes V_1 \otimes Z)vec(C)$ in the tensor format as $\tilde{Y} = \tilde{C} \times_1 Z \times_2 V_1 \times \dots \times_{d+1} V_d$, which can be written as $\tilde{Y}_{(i)} = V_i \tilde{C}_{(i)} (V_d \otimes \dots \otimes V_{i+1} \otimes V_{i-1} \otimes V_1 \otimes Z)^T$. First note that

$$\begin{aligned} \operatorname{argmin}_{V_i} \|Y_{(1)} - X_{(1)}B\|_F^2 &= \operatorname{argmin}_{V_i} \|vec(Y_{(1)}) - (V_d \otimes \dots \otimes V_1 \otimes Z)vec(\tilde{C})\|_F^2 \\ &= \operatorname{argmin}_{V_i} \|Y_{(i)} - \tilde{Y}_{(i)}\|_F^2 \\ &= \operatorname{argmin}_{V_i} \|Y_{(i)} - V_i \tilde{C}_{(i)} (V_d \otimes \dots \otimes V_{i+1} \otimes V_{i-1} \otimes V_1 \otimes Z)^T\|_F^2, \end{aligned}$$

with $A := \tilde{C}_{(i)} (V_d \otimes \dots \otimes V_{i+1} \otimes V_{i-1} \otimes V_1 \otimes Z)^T$. Then, we want to solve

$$\operatorname{argmin}_{V_i} \|Y_{(i)} - V_i A\|_F^2 \text{ s.t. } V_i^T V_i = I.$$

This is an orthogonal procrustes problem and is known to have solution as is stated in Proposition 3.

Appendix C: Simulating the Overlay Error

Brunner *et al.* (2013) introduced a measure based on in-plane distortion (IPD) called predicted in-plane distortion residual (PIR) to estimate and predict nonuniform-stress-induced overlay errors based on wafer shape. For this purpose, they first illustrate that the IPD is proportional to gradient of wafer shape $w(x, y)$, i.e.,

$$IPD \propto -\nabla w.$$

Then, for two layers, say i and k , to be patterned, they calculate the IPD and subtract them to find the shape-slope difference, i.e., $SSD = IPD_i - IPD_k$. The shape-slope is then corrected based on

model (8) to find the shape-slope residual (SSR). Finally, Brunner *et al.* (2013) calculated the PIR as a factor of SSR. That is,

$$PIR = c \times SSR,$$

where c is a constant that depends on the wafer thickness. In their study, they showed through four differently patterned engineer stress monitor (ESM) wafers that the PIR is linearly correlated by the overlay errors with high R^2 values (e.g., 92%). To perform the experiment, they first deposit a layer of silicon nitride film over a 300mm wafer as a source of stress. This process changes the wafer shape and causes the wafer to curve. The shape of the wafer is measured by a patterned wafer geometry (PWG) tool designed for the metrology of 300mm wafers. After the wafer is exposed by a designed pattern (four different patterns considered in this study), it goes through an etching process that relieves some part of the stress depending on the pattern density. At this stage, and prior to next lithography step, the wafer shape is again measured. After the second lithography step, the overlay error is measured using standard optical methods. Using the measured wafer shapes, they calculated the PIR and showed a high correlation between the PIR and overlay error.

In our study, we first simulate the wafer shapes and then estimate the overlay errors using the following procedure introduced by Brunner *et al.* (2013). Simulating a wafer shape requires knowledge of the different components in wafer geometry. Brunner *et al.* (2013) and Turner *et al.* (2013) consider several wafer shape features that span different ranges of spatial wavelength (λ). At the highest level is the overall shape of the wafer represented by a bow (or warp) in the range of tens of micrometers. Other shape variations are those that are spanned by spatial wavelengths in the range of several meters and waveheight in the micrometer range. Another component is the nanotopography (NT) of the wafer, with λ ranging from few millimeters to 20mm and the waveheight in nanometers. Finally, the roughness of the wafer is defined as variations with $\lambda < 0.2\text{mm}$. In this study, we only consider the bow shape and the NT components when simulating a wafer shape. The wafer shapes are simulated as follows: We first assume that a thin layer is deposited over a wafer, which causes only a bow shape geometry in the wafer (that is, we assume no wave patterns). We simulate the bowed wafer geometry using $w_1(x, y) = \frac{b_1(0.5x^2 + y^2)}{R^2}$, where b_1 is the warp or bow size and is assumed to be $100\mu\text{m}$, and R is the wafer radius, which is assumed to be 150mm . We then assume that a lithography/etching process is performed and the wafer shape

changes in both bow and wavy patterns as follows:

$$w_2(x, y) = \frac{b_2(0.5x^2 + y^2)}{R^2} + \sum_{i=1}^p \frac{h_i}{2} \left(1 + \sin\left(\frac{2\pi x}{\lambda_i}\right) \right) + \sum_{i=1}^p \frac{h_i}{2} \left(1 + \cos\left(\frac{2\pi y}{\lambda_i}\right) \right),$$

where b_2 is the bow size uniformly sampled from 30 to $100\mu m$, and h_i and λ_i are the waveheight and wavelength, respectively. Moreover, p is the number of waveforms assumed. For each wafer (i.e. sample), we first randomly select p from $U(2, 10)$ and then select p wavelength from $U(2, 20)$ for NT wavelength. Finally, we sample waveheight h_i from $U\left(\frac{\lambda_i}{10^7}, \frac{\lambda_i}{10^6}\right)$ to ensure that the large wavelength has large a waveheight and vice versa. After simulating a wafer shape prior to two lithography steps, we calculate the IPD and PIR according to the procedure described previously. Note that we only calculate the values proportional to the original values. Figure 9 illustrates an example of generated shapes, their associated IPDs in the x coordinates, i.e., $-\frac{\partial w}{\partial x}$, and the difference between the x coordinate IPDs prior to and after correction. In order to correct the IPD values, we consider a second order model:

$$\begin{cases} \Delta IPD_x = k_0 + k_1x + k_2y + k_3x^2 + k_4y^2 + k_5xy & \text{error in x coordinate} \\ \Delta IPD_y = k_6 + k_7x + k_8y + k_9x^2 + k_{10}y^2 + k_{11}xy & \text{error in y coordinate,} \end{cases}$$

which is fitted to the calculated values of $\Delta IPD_x = IPD_{x2} - IPD_{x1}$ and ΔIPD_y . Then the fitted model is subtracted from the ΔIPD_x and ΔIPD_y to find the corrected values. The corrected values are associated with the PIR and the overlay error.

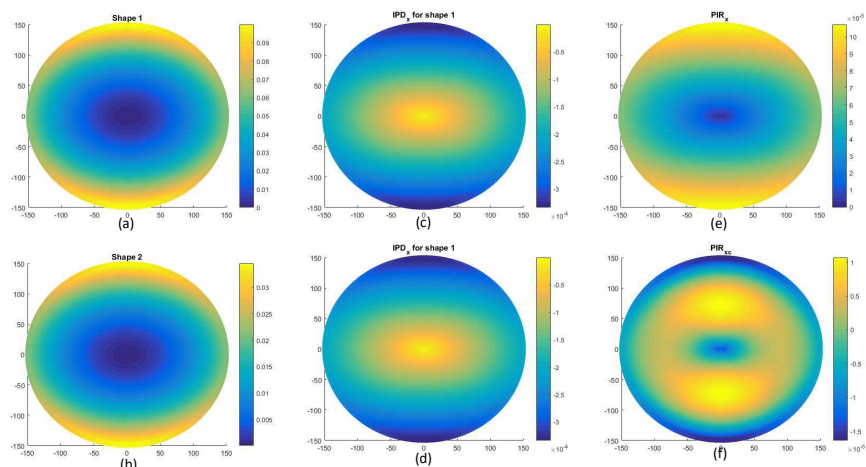


Figure 9: Illustration of wafer (a) shape prior to first step lithography, (b) shape prior to second step lithography, (c) IPD_x for the first shape, (d) IPD_x for the second shape, (e) PIR prior to correction, and (f) PIR after correction for second order shapes.

References

- BALAGEAS, DANIEL, FRITZEN, CLAUS-PETER, & GÜEMES, ALFREDO. 2010. *Structural Health Monitoring*. Vol. 90. John Wiley & Sons.
- BECK, AMIR, & TBOULLE, MARC. 2009. A fast iterative shrinkage-thresholding algorithm for linear inverse problems. *SIAM Journal on Imaging Sciences*, **2**(1), 183–202.
- BELLON, E, VAN CLEYNENBREUGEL, J, DELAERE, D, HOUTPUT, W, SMET, M, MARCHAL, G, & SUETENS, P. 1995. Experimental teleradiology. novel telematics services using image processing, hypermedia and remote cooperation to improve image-based medical decision making. *Journal of Telemedicine and Telecare*, **1**(2), 100–110.
- BRUNNER, TIMOTHY A, MENON, VINAYAN C, WONG, CHEUK WUN, GLUSCHENKOV, OLEG, BELYANSKY, MICHAEL P, FELIX, NELSON M, AUSSCHNITT, CHRISTOPHER P, VUKKADALA, PRADEEP, VEERARAGHAVAN, SATHISH, & SINHA, JAYDEEP K. 2013. Characterization of wafer geometry and overlay error on silicon wafers with nonuniform stress. *Journal of Micro/Nanolithography, MEMS, and MOEMS*, **12**(4), 043002–043002.

- CHIOU, JENG-MIN, MÜLLER, HANS-GEORG, & WANG, JANE-LING. 2004. Functional response models. *Statistica Sinica*, 675–693.
- FAN, YINGYING, FOUTZ, NATASHA, JAMES, GARETH M, JANK, WOLFGANG, *et al.* 2014. Functional response additive model estimation with online virtual stock markets. *The Annals of Applied Statistics*, **8**(4), 2435–2460.
- GORGANNEJAD, SANAM, REISI GAHROOEI, MOSTAFA, PAYNABAR, KAMRAN, & NEU, RICHARD W. 2018. Characterizing the aged state of Ni-based superalloys based on process variables using PCA and tensor regression. *Acta Materialia*, **submitted**.
- HE, G, MÜLLER, HG, & WANG, JL. 2000. Extending correlation and regression from multivariate to functional data. *Asymptotics in Statistics and Probability*, 197–210.
- IVANESCU, ANDRADA E, STAIKU, ANA-MARIA, SCHEIPL, FABIAN, & GREVEN, SONJA. 2015. Penalized function-on-function regression. *Computational Statistics*, **30**(2), 539–568.
- KHOSRAVANI, ALI, CECEN, AHMET, & KALIDINDI, SURYA R. 2017. Development of high throughput assays for establishing process-structure-property linkages in multiphase polycrystalline metals: Application to dual-phase steels. *Acta Materialia*, **123**, 55–69.
- KIERS, HENK AL. 2000. Towards a standardized notation and terminology in multiway analysis. *Journal of Chemometrics*, **14**(3), 105–122.
- KOLDA, TAMARA GIBSON. 2006. *Multilinear operators for higher-order decompositions*. Tech. rept. Sandia National Laboratories.
- LI, XIAOSHAN, ZHOU, HUA, & LI, LEXIN. 2013. Tucker tensor regression and neuroimaging analysis. *arxiv preprint arxiv:1304.5637*.
- LIANG, HUA, WU, HULIN, & CARROLL, RAYMOND J. 2003. The relationship between virologic and immunologic responses in AIDS clinical research using mixed-effects varying-coefficient models with measurement error. *Biostatistics*, **4**(2), 297–312.
- LOCK, ERIC F. 2017. Tensor-on-tensor regression. *arxiv preprint arxiv:1701.01037*.

- LUO, RUIYAN, & QI, XIN. 2017. Function-on-function linear regression by signal compression. *Journal of the American Statistical Association*, 1–16.
- NISHI, YOSHIO, & DOERING, ROBERT. 2000. *Handbook of Semiconductor Manufacturing Technology*. CRC Press.
- RAMSAY, JAMES, & SILVERMAN, BW. 2005. *Functional Data Analysis*. Springer Science & Business Media.
- SAPIENZA, ANNA, PANISSON, ANDRÉ, WU, JOSEPH, GAUVIN, LAETITIA, & CATTUTO, CIRO. 2015. Detecting anomalies in time-varying networks using tensor decomposition. *Pages 516–523 of: IEEE International Conference on data Mining Workshop (ICDMW)*.
- SHARAN, VATSAL, & VALIANT, GREGORY. 2017. Orthogonalized ALS: A theoretically principled tensor decomposition algorithm for practical use. *arxiv preprint arxiv:1703.01804*.
- SUN, JIMENG, PAPADIMITRIOU, SPIROS, & PHILIP, S YU. 2006. Window-based tensor analysis on high-dimensional and multi-aspect streams. *Pages 1076–1080 of: ICDM*.
- SZATVANYI, G, DUCHESNE, C, & BARTOLACCI, G. 2006. Multivariate image analysis of flames for product quality and combustion control in rotary kilns. *Industrial & Engineering Chemistry Research*, **45**(13), 4706–4715.
- TUCKER, LEDYARD R. 1963. Implications of factor analysis of three-way matrices for measurement of change. *Problems in Measuring Change*, **122137**.
- TURNER, KEVIN T, RAMKHALAWON, ROSHITA, & SINHA, JAYDEEP K. 2013. Role of wafer geometry in wafer chucking. *Journal of Micro/Nanolithography, MEMS, and MOEMS*, **12**(2), 023007–023007.
- WÓJCIK, WALDEMAR, & KOTYRA, ANDRZEJ. 2009. Combustion diagnosis by image processing. *Photonics Letters of Poland*, **1**(1), 40–42.
- YAN, HAO, PAYNABAR, KAMRAN, & SHI, JIANJUN. 2015. Image-based process monitoring using low-rank tensor decomposition. *IEEE Transactions on Automation Science and Engineering*, **12**(1), 216–227.

- YAN, HAO, PAYNABAR, KAMRAN, & PACELLA, MASSIMO. 2017. Structured point cloud data analysis for process modeling and optimization. *Technometrics*, **submitted**.
- YAO, FANG, MÜLLER, HANS-GEORG, WANG, JANE-LING, *et al.* 2005. Functional linear regression analysis for longitudinal data. *The Annals of Statistics*, **33**(6), 2873–2903.
- YU, HONGLU, & MACGREGOR, JOHN F. 2003. Multivariate image analysis and regression for prediction of coating content and distribution in the production of snack foods. *Chemometrics and Intelligent Laboratory Systems*, **67**(2), 125–144.
- ZHOU, HUA, LI, LEXIN, & ZHU, HONGTU. 2013. Tensor regression with applications in neuroimaging data analysis. *Journal of the American Statistical Association*, **108**(502), 540–552.